IEEE Access
Multidisciplinary ⁝ Rapid Review ⁝ Open Access Journal

Received October 24, 2021, accepted November 7, 2021, date of publication November 15, 2021, date of current version November 22, 2021.

Digital Object Identifier 10.1109/ACCESS.2021.3128215

A Sliding-Mode Set-Point Position Controller for Hydraulic Excavators

YUKI YAMAMOTO[1], JINJUN QIU[2], YOSHIKI MUNEMASA[2], TAKAYUKI DOI[2], TAKAO NANJO[2], KOJI YAMASHITA[2], AND RYO KIKUUWE[1], (Member, IEEE)

[1]Machinery Dynamics Laboratory, Hiroshima University, Higashihiroshima, Hiroshima 739-8527, Japan
[2]Kobelco Construction Machinery Company Ltd., Saeki-ku, Hiroshima 731-5161, Japan

Corresponding author: Yuki Yamamoto (y.yamamoto@mdl.hiroshima-u.ac.jp)

This work was supported by Kobelco Construction Machinery Company Ltd., Hiroshima, Japan.

ABSTRACT This paper proposes a sliding-mode set-point position controller for hydraulic excavators. The controller employs a simple switching surface that exponentially drives the actuator position to the desired position with a specified time constant. The discrete-time algorithm of the controller is constructed through a double-implicit implementation scheme, which is for implementing a simple sliding-mode controller to nonsmooth actuators, including hydraulic actuators. We employ a nonsmooth quasistatic model of the hydraulic actuator, which analytically accounts for the pressure saturation caused by the relief valves and check valves and the square-root law of the pressure-flowrate relation. This paper elaborates the analytical form of the model to be combined with the double-implicit implementation. A state predictor based on the actuator model extends the controller to compensate for the deadtime in the hydraulic system. The proposed controller is validated with some simulations and also through experiments employing the swing axis of a 13-ton class excavator.

INDEX TERMS Deadtime compensation, hydraulic actuator, hydraulic excavator, sliding-mode control.

I. INTRODUCTION

Hydraulic excavators are expected to expand their applicability through the combination with more sophisticated control technology. In particular, automatic, semi-automatic, and teleoperated excavators would be potentially useful in many applications such as construction, disaster restoration, and demolition. Position control technology of hydraulic actuators is an essential building block for such future applications. There have been many position controllers proposed for hydraulic actuators. Many of them are intended for trajectory-tracking control [1]–[6], with which the actuator tracks time-varying position command. In many of the reported experimental results, the excavators track smooth command trajectories without making large positional errors.

In contrast to the trajectory-tracking problem, the set-point control problem, i.e., position control from large positional errors, is also important for semi-automatic or teleoperated hydraulic excavators. Such large positional errors may happen when the desired position discontinuously jumps due to communication failures or in applications where the excavator is commanded to move its bucket back to a registered position. The practical requirement for set-point control of excavators is not only to ensure accurate convergence but also to realize appropriate transient behavior converging to the desired position without producing oscillation or overshoots.

Some previous papers [7]–[11] report experimental results of transient responses to a step-like position command. Many of these papers employ proportional-integral-derivative (PID) controllers with which the control gains are adjusted with numerical, heuristic, or empirical methods, such as particle swarm optimization method [7], [8], genetic algorithm [9], and ant-colony optimization [10]. Kim *et al.* [11] approach is based on an analytical model of the hydraulic system, being based on a linearized system model with multiplicative uncertainty. As far as the authors are aware, there have been no set-point control methods that analytically account for the nonlinearity of the hydraulic systems, such as the pressure saturation caused by the relief valves and check valves, and the square-root law (see, e.g., [12]) of the pressure-flowrate relation.

One convenient approach to design the transient behavior of set-point control is to employ the concept of sliding-mode control, which constrains the system state to the prescribed convergence law. Sliding-mode control is also convenient

The associate editor coordinating the review of this manuscript and approving it for publication was Shen Yin.

to deal with saturation because the bounds of the control input can be explicitly specified in the controller structure. The use of sliding-mode control from this perspective has been proposed for robotic manipulators [13], [14] but not for hydraulic systems. Previous sliding-mode controllers for hydraulic excavators [1], [5], [6] are for ensuring accurate convergence to the desired position, not for designing the transient behavior.

This paper presents a sliding-mode set-point position controller for hydraulic excavators. The controller employs a simple switching surface that exponentially drives the actuator position to the desired position with a specified time constant. The discrete-time algorithm of the controller is constructed through a double-implicit implementation scheme [15], which is for implementing a simple sliding-mode controller to a particular class of plants. We employ a nonsmooth quasistatic model [16] of the actuator structure illustrated in Fig. 1. This paper elaborates the analytical form of the nonsmooth quasistatic model to be combined with the double-implicit implementation and also extends the controller by a model-based state predictor to compensate for the deadtime in the plant. The controller is tested with simulations and experiments employing the swing axis of a 13-ton class excavator.

One practical benefit of the proposed controller is that most of the parameters can be uniquely chosen according to the hardware specifications, without the necessity of parameter tuning on a trial-and-error basis. It is in contrast to simple linear controllers such as PD, PI, or PID controllers. It may be possible to establish gain-tuning methods for linear controllers based on locally linearized models [11], [17], [18], but they do not cope with strong nonlinearity or nonsmoothness in the relation between the control input and the actuator force, which are caused by relief valves and check valves. Being based on the double-implicit implementation framework [15], our approach fully accounts for nonlinear factors that are not suited for local linearization, such as the pressure saturation caused by the relief and check valves and the square-root law between the valve flowrate and the pressure drop.

The rest of this paper is organized as follows. Section II provides preliminaries, including the nonsmooth quasistatic model [16] of a hydraulic actuator and the double-implicit implementation [15] of a sliding-mode controller. Section III presents the proposed controller for excavators, which is based on the nonsmooth quasistatic model and the double-implicit implementation, and comprises the state predictor to compensate for the deadtime in the plant. Section IV and Section V presents simulation and experimental results, respectively. Section VI concludes this paper.

II. PRELIMINARIES

A. MATHEMATICAL PRELIMINARIES

In this paper, $\mathbb{R}$ denotes the set of all real numbers, $\overline{\mathbb{R}}$ denotes the set of extended real numbers,

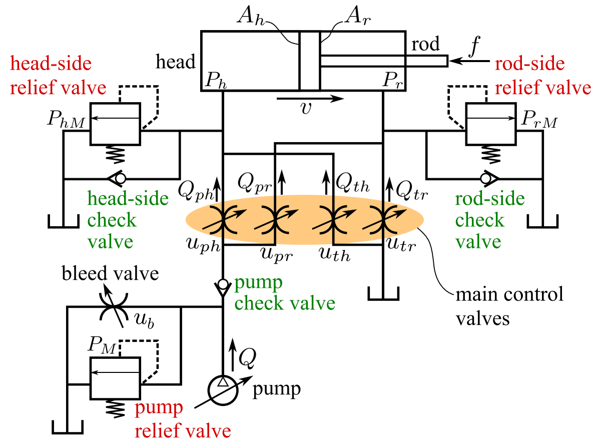

FIGURE 1. Hydraulic actuator and its circuit.

i.e., $\overline{\mathbb{R}} \triangleq \mathbb{R} \cup \{-\infty, +\infty\}$, $\mathbb{R}_+$ denotes the set of all non-negative real numbers, $\mathbb{R}_-$ denotes the set of all non-positive real numbers, and $\mathcal{B}$ denotes the closed unit ball in $\mathbb{R}$, i.e., $\mathcal{B} \triangleq [-1, 1] \subset \mathbb{R}$.

The following functions are used in this paper:

$$\mathrm{sat}_{\mathcal{X}}(x) \triangleq \begin{cases} \min \mathcal{X} & \text{if } x < \min \mathcal{X} \\ x & \text{if } x \in \mathcal{X} \\ \max \mathcal{X} & \text{if } x > \max \mathcal{X} \end{cases} \tag{1}$$

$$\mathrm{sgn}(x) \triangleq \begin{cases} x/|x| & \text{if } x \neq 0 \\ [-1, 1] & \text{if } x = 0 \end{cases} \tag{2}$$

$$\mathrm{gsgn}(a, x, b) \triangleq \begin{cases} b & \text{if } x > 0 \\ \mathrm{conv}\{a, b\} & \text{if } x = 0 \\ a & \text{if } x < 0 \end{cases} \tag{3}$$

$$\mathcal{S}(x) \triangleq \mathrm{sgn}(x)x^2 \tag{4}$$

$$\mathcal{R}(x) \triangleq \mathrm{sgn}(x)\sqrt{|x|} \tag{5}$$

$$\mathcal{N}_{\mathcal{X}}(x) \triangleq \begin{cases} [0, \infty] & \text{if } x = \max \mathcal{X} \\ 0 & \text{if } x \in \mathcal{X}^\circ \\ [-\infty, 0] & \text{if } x = \min \mathcal{X} \\ \emptyset & \text{if } x \notin \mathcal{X} \end{cases} \tag{6}$$

where $\mathcal{X}$ is a closed interval in $\overline{\mathbb{R}}$, and $\mathcal{X}^\circ$ is the interior of $\mathcal{X}$. Here, $\mathrm{conv}\{a, b\}$ stands for the convex closure of the set $\{a, b\}$, being the closed set $[a, b]$ if $a \leq b$ and $[b, a]$ if $b \leq a$. In addition, the following relation holds true between the functions $\mathcal{N}$ and sgn:

$$y \in \mathcal{N}_{\mathcal{B}}(x) \iff x \in \mathrm{sgn}(y). \tag{7}$$

A function of one or more sets should be understood in the following manner:

$$\Phi(\mathcal{X}) = \bigcup_{x \in \mathcal{X}} \Phi(x) \tag{8}$$

$$\Phi(\mathcal{X}, \mathcal{Y}) = \bigcup_{\{x,y\} \in \mathcal{X} \times \mathcal{Y}} \Phi(x, y). \tag{9}$$

With a set-valued function $f : \mathcal{C}_x \rightrightarrows \mathcal{C}_y$ where $\mathcal{C}_x \subset \overline{\mathbb{R}}$ and $\mathcal{C}_y \subset \overline{\mathbb{R}}$, recall that the inverse function $f^{-1} : \mathcal{C}_y \rightrightarrows \mathcal{C}_x$ is the function that satisfies the following condition:

$$y \in f(x) \iff x \in f^{-1}(y), \quad \forall\{x, y\} \in \mathcal{C}_x \times \mathcal{C}_y. \tag{10}$$

A set-valued function $f : \mathcal{C}_x \rightrightarrows \mathcal{C}_y$ is said to be total if $f(x) \neq \emptyset$ for all $x \in \mathcal{C}_x$. It is said to be surjective if, for all $y \in \mathcal{C}_y$, there exists $x \in \mathcal{C}_x$ such that $y \in f(x)$. If f is total and surjective, f^{-1} is also total and surjective. A set-valued function f is said to be monotone if it satisfies $(x_1 - x_2)(y_1 - y_2) \geq 0$ for all $x_1, x_2 \in \mathcal{C}_x$, $y_1 \in f(x_1)$, and $y_2 \in f(x_2)$. With a monotone function f, the following is satisfied:

$$f(x_1) \ni y_1 \leq y_2 \in f(x_2) \iff f^{-1}(y_1) \ni x_1 \leq x_2 \in f^{-1}(y_2). \tag{11}$$

This paper defines set-valued extensions of min and max operators as follows:

$$\max(\mathcal{X}, \mathcal{Y}) \triangleq \{\xi \in \overline{\mathbb{R}} \mid \mathcal{X} \ni \xi \geq \exists y \in \mathcal{Y} \ \vee \ \mathcal{X} \ni \exists x \leq \xi \in \mathcal{Y}\} \tag{12a}$$

$$\min(\mathcal{X}, \mathcal{Y}) \triangleq \{\xi \in \overline{\mathbb{R}} \mid \mathcal{X} \ni \xi \leq \exists y \in \mathcal{Y} \ \vee \ \mathcal{X} \ni \exists x \geq \xi \in \mathcal{Y}\} \tag{12b}$$

where $\mathcal{X} \subset \overline{\mathbb{R}}$ and $\mathcal{Y} \subset \overline{\mathbb{R}}$. If $\mathcal{X}$ and $\mathcal{Y}$ are closed intervals in $\overline{\mathbb{R}}$, the followings are satisfied:

$$\max(\mathcal{X}, \mathcal{Y}) = [\max(\min \mathcal{X}, \min \mathcal{Y}), \max(\max \mathcal{X}, \max \mathcal{Y})] \tag{13a}$$

$$\min(\mathcal{X}, \mathcal{Y}) = [\min(\min \mathcal{X}, \min \mathcal{Y}), \min(\max \mathcal{X}, \max \mathcal{Y})]. \tag{13b}$$

The following lemma is useful to deal with the inverse functions and the min and max operators.

Lemma 1: Let $f_1 : \mathcal{C} \rightrightarrows \overline{\mathbb{R}}$ and $f_2 : \mathcal{C} \rightrightarrows \overline{\mathbb{R}}$ be total, surjective, monotone, set-valued functions where $\mathcal{C} \subset \overline{\mathbb{R}}$. Then, $f(x) \triangleq \min(f_1(x), f_2(x))$ results in $f^{-1}(y) = \max(f_1^{-1}(y), f_2^{-1}(y))$ and $f(x) \triangleq \max(f_1(x), f_2(x))$ results in $f^{-1}(y) = \min(f_1^{-1}(y), f_2^{-1}(y))$.

Proof: See Appendix A. □

B. NONSMOOTH QUASISTATIC MODEL OF A HYDRAULIC ACTUATOR

This section overviews the nonsmooth quasistatic model [16] of the hydraulic actuator driven by the circuit illustrated in Fig. 1. As can be seen in the figure, the actuator has two chambers separated by a piston, and the circuit has four main control valves, a bleed valve, three relief valves, and three check valves. The cross-sectional areas and the internal pressures of the chambers are denoted by A_* and P_* ($* \in \{h, r\}$), respectively, where h means the head-side and r means the rod-side. The pressure limits of the head- and rod-side relief valves are P_{hM} and P_{rM}, respectively. The oil flow in the circuit is supplied by a single pump, of which the flowrate is Q. The circuit comprises a pump relief valve, of which the pressure limit is P_M, to secure the oil outlet from the pump, and a pump check valve to prevent the backflow into the pump.

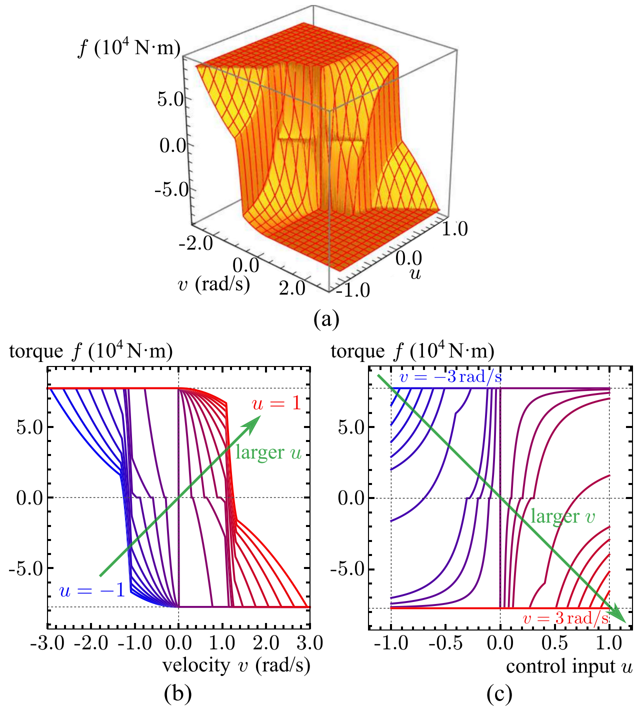

FIGURE 2. A numerical example of the quasistatic model $f \in \Gamma(v, u)$ defined in [16]; (a) three-dimensional surface plot, (b) cross-sectional plots at some u values, and (c) cross-sectional plots at some v values. The function is set-valued at $v = 0$ and $u = 0$. An alternative analytical form of Γ is given in (24).

For each of the control valves (four main control valves and one bleed valve), the ratio of the valve opening area to its maximum value is denoted by $u_* \in [0, 1]$ ($* \in \{ph, pr, th, tr, b\}$). The flowrates Q_* ($* \in \{ph, pr, th, tr, b\}$) through the valves can be assumed to satisfy the following flowrate-pressure relations [12], [19]:

$$Q_* = c_* u_* \mathcal{R}(\Delta P_*) \ (* \in \{ph, tr, th, pr, b\}) \tag{14}$$

where $c_* \triangleq C_* a_* \sqrt{2/\rho}$, ΔP_* is the pressure drop across the valve, ρ is the mass density of the oil, a_* is the maximum opening area of the valve, and C_* is the discharge coefficient [20] of the valve. The discharge coefficient C_* is a dimensionless quantity of which the value is typically around 0.6 or 0.7 [21], [22].

The nonsmooth quasistatic model gives the algebraic relation among the actuator force f, the ratios of the valve opening areas $u_* \in [0, 1]$ ($* \in \{ph, pr, th, tr, b\}$), and the velocity v. For simplicity, the ratios $u_* \in [0, 1]$ ($* \in \{ph, pr, th, tr\}$) can be assumed to be determined by a control input $u \in \mathcal{B}$ as follows:

$$u_{ph} = u_{tr} = \max(0, u), \quad u_{pt} = u_{th} = -\min(0, u). \tag{15}$$

The model with this control input u can be represented by a set-valued (thus nonsmooth) function $\Gamma : \mathbb{R} \times \mathcal{B} \rightrightarrows \mathbb{R}$, with which f, v and u are constrained in the form $f \in \Gamma(v, u)$. The complete analytical expression of the function Γ is presented in [16]. Fig. 2 illustrates a numerical example of the function Γ with the parameter values detailed in Section IV.

C. DOUBLE-IMPLICIT IMPLEMENTATION OF NONSMOOTH CONTROLLERS

This section gives an overview of the double-implicit implementation scheme proposed in [15], which is for implementing a sliding-mode controller to a plant driven by a nonsmooth actuator. It is an extension of the implicit implementation scheme [23]–[28], which is to implement a nonsmooth controller, such as a sliding-mode controller, to a smooth plant, which can be described by an ordinary differential equation. The implicit implementation scheme employs the implicit Euler discretizations of the controller and the plant to construct a discrete-time algorithm of the controller that does not produce chattering. The double-implicit implementation scheme [15] is its extension to deal with the case where both controller and plant are nonsmooth.

The double-implicit implementation scheme is to deal with the position control of plants that can be written in the following form:

$$M\dot{v} = f + g \tag{16a}$$
$$v = \dot{p} \tag{16b}$$
$$f \in \Gamma(v, u) \tag{16c}$$

where $p \in \mathbb{R}$, $v \in \mathbb{R}$, and $M \in \mathbb{R}_+$ are the position, the velocity, and the mass of the controlled object, respectively. The controlled object is subjected to the external force $g \in \mathbb{R}$ and the actuator force $f \in \mathbb{R}$, and the force f is generated by the actuator modeled as a nonsmooth function $\Gamma : \mathbb{R} \times \mathcal{B} \rightrightarrows \mathbb{R}$. Here, $u \in \mathcal{B}$ is the control input that should be given to the actuator from a controller.

For the position control of the plant (16), a simple sliding-mode controller of the following form is considered:

$$f \in \Gamma\left(v, \operatorname{sgn}(p_d - p - Hv)\right) \tag{17}$$

where $p_d \in \mathbb{R}$ is the desired position and $H > 0$ is a parameter for the controller. The control input u in (16c) should be chosen so that (17) is realized. Theorem 2 in [15] suggests that, with this controller, the sliding mode can be established on the switching surface $\sigma \triangleq p - p_d + Hv = 0$ and thus p exponentially converges to p_d with the time constant H.

In the double-implicit implementation scheme, a discrete-time algorithm that realizes the controller (17) combined with the plant (16) is derived. It is based on the implicit Euler discretization of the nominal model of the plant (16) and the controller (17), which are written as follows:

$$M(v_{k+1} - v_k)/T = f_k + g_k \tag{18a}$$
$$v_{k+1} = (p_{k+1} - p_k)/T \tag{18b}$$
$$f_k \in \Gamma(v_{k+1}, u_k) \tag{18c}$$
$$f_k \in \Gamma(v_{k+1}, \operatorname{sgn}(p_d - p_{k+1} - Hv_{k+1})). \tag{18d}$$

Here, T denotes the sampling interval and k denotes the discrete-time index. The control input u_k needs to be obtained from the set of algebraic constraints (18) according to the inputs p_k, v_k, and g_k.

Through tedious but straightforward algebraic manipulations on (18), one obtains the following algorithm to obtain u_k:

$$v_{f,k} := v_k + g_k T/M \tag{19a}$$
$$v_{s,k} := (p_d - p_k)/(H + T) \tag{19b}$$
$$f_k := \operatorname{sat}_{\Gamma_s(T/M, v_{f,k}, \mathcal{B})}((v_{s,k} - v_{f,k})M/T) \tag{19c}$$
$$u_k := \Theta_s(v_{f,k} + f_k T/M, f_k) \tag{19d}$$

where Γ_s and Θ_s are functions that satisfy the followings:

$$f = \Gamma_s(\eta, v, u) \iff f \in \Gamma(v + \eta f, u) \tag{20}$$
$$u \in \Theta(v, f) \iff f \in \Gamma(v, u) \tag{21}$$
$$\Theta_s(v, f) \in \Theta\left(v, \operatorname{sat}_{\Gamma(v,\mathcal{B})}(f)\right) \tag{22}$$

where $\eta > 0$. Here, Γ_s is a single-valued function that is uniquely defined by (20) as detailed in Theorem 3 in [15], Θ is the inverse function of Γ with respect to its second argument, and Θ_s is a single-valued selection of Θ. Although Θ_s is not unique, its use in the algorithm can be justified by Theorem 1 in [15]. The previous paper [15] provides the algorithm (19) and the relations (20), (21), and (22), but does not provide the analytical expressions of Γ_s, Θ or Θ_s corresponding to the function Γ presented in [16].

As for the algorithm (19), it should be noted that $v_{f,k} + f_k T/M$, which is in (19d), can be interpreted as the velocity predicted to be achieved in the next timestep if the desired force f_k is kept by the actuator for the time period $t \in [kT, (k+1)T)$.

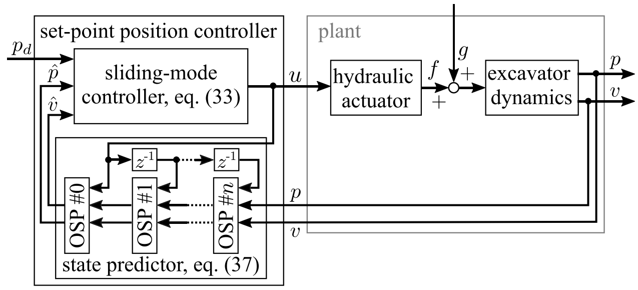

FIGURE 3. Block diagram of the proposed controller. The OSP stands for a one-step predictor. The sliding-mode controller is implementated by the double-implicit implementation scheme [15].

III. SET-POINT POSITION CONTROLLER FOR HYDRAULIC EXCAVATORS

This section proposes a set-point position controller for hydraulic excavators. Fig. 3 illustrates the overall structure of the controller. The proposed controller consists of a sliding-mode controller and a state predictor to compensate for the deadtime. The sliding-mode controller is implemented through the double-implicit implementation scheme [15], which requires the inverse model of the actuator. This section derives the inverse model of the nonsmooth quasistatic model [16] and presents the controller algorithm.

The algorithm of the state predictor is also presented in this section.

A. INVERSION OF THE NONSMOOTH QUASISTATIC MODEL

As overviewed in Section II-B, the actuator model is represented by a function $\Gamma : \mathbb{R} \times \mathcal{B} \rightrightarrows \mathbb{R}$, of which the complete analytical form is given in [16]. This section gives the analytical form of its inverse function Θ with respect to the second argument, which satisfies (21).

For the convenience of the derivation of the function Θ, we rewrite the function Γ in an expression different from that in [16]. To this end, let us define functions $\gamma_+ : (1+\varepsilon)\mathcal{B}\times\mathbb{R}_+\times\mathbb{R} \rightrightarrows \overline{\mathbb{R}}$ and $\gamma_- : (1+\varepsilon)\mathcal{B}\times\mathbb{R}_-\times\mathbb{R} \rightrightarrows \overline{\mathbb{R}}$ as follows:

$$\gamma_+(u; \bar{v}, a) \triangleq a + \mathcal{N}_{(1+\varepsilon)\mathcal{B}}(u) + \begin{cases} -\dfrac{\mathcal{S}(\bar{v})}{u^2} & \text{if } u\bar{v} > 0 \vee (u \neq 0 \wedge \bar{v} = 0) \\ -\infty & \text{if } u \leq 0 \wedge \bar{v} > 0 \\ [-\infty, 0] & \text{if } u = 0 \wedge \bar{v} = 0 \end{cases} \tag{23a}$$

$$\gamma_-(u; \bar{v}, a) \triangleq a + \mathcal{N}_{(1+\varepsilon)\mathcal{B}}(u) + \begin{cases} -\dfrac{\mathcal{S}(\bar{v})}{u^2} & \text{if } u\bar{v} > 0 \vee (u \neq 0 \wedge \bar{v} = 0) \\ +\infty & \text{if } u \geq 0 \wedge \bar{v} < 0 \\ [0, +\infty] & \text{if } u = 0 \wedge \bar{v} = 0. \end{cases} \tag{23b}$$

Here, ε is a positive scalar satisfying $0 < \varepsilon \ll 1$. These functions are monotone with respect to the first argument $u \in (1+\varepsilon)\mathcal{B}$, and are single-valued as long as $u \in \mathcal{B}$. The domain of the first argument of $\gamma_\pm$ is $(1+\varepsilon)\mathcal{B}$, which is set slightly larger than $\mathcal{B}$ to make $\gamma_\pm$ to be surjective from $u \in (1+\varepsilon)\mathcal{B}$ to $f \in \overline{\mathbb{R}}$. Setting them surjective is for the convenience of employing their inverse functions and Lemma 1.

Using the functions $\gamma_\pm$ defined in (23), the function $\Gamma : \mathbb{R} \times \mathcal{B} \rightrightarrows \overline{\mathbb{R}}$ defined in [16] can be equivalently rewritten as follows:

$$\Gamma(v, u) \triangleq \operatorname{gsgn}(\Gamma_-(v, u), v, \Gamma_+(v, u)) \tag{24a}$$

where $\Gamma_* : \mathbb{R} \times (1+\varepsilon)\mathcal{B} \rightrightarrows \overline{\mathbb{R}}$ are defined as follows:

$$\begin{aligned}\Gamma_+(v, u) \triangleq \max\big(&\min\big(\max\left(\Gamma_{+0a}(v, u), \Gamma_{+0b}(v, u)\right), \\ &\max\left(\Gamma_{+1a}(v, u), \Gamma_{+1b}(v, u)\right), \max\left(\Gamma_{+2a}(v, u),\right. \\ &\left.\Gamma_{+2b}(v, u)\right)\big), \Gamma_{+3a}(v, u), \Gamma_{+3b}(v, u)\big)\end{aligned} \tag{24b}$$

$$\begin{aligned}\Gamma_-(v, u) \triangleq \min\big(&\max\big(\min\left(\Gamma_{-0a}(v, u), \Gamma_{-0b}(v, u)\right), \\ &\min\left(\Gamma_{-1a}(v, u), \Gamma_{-1b}(v, u)\right), \min\left(\Gamma_{-2a}(v, u),\right. \\ &\left.\Gamma_{-2b}(v, u)\right)\big), \Gamma_{-3a}(v, u), \Gamma_{-3b}(v, u)\big)\end{aligned} \tag{24c}$$

and

$$\Gamma_{+0a}(v, u) \triangleq \gamma_+(u; C_{tr}v, F_{hM}) \tag{24d}$$
$$\Gamma_{+0b}(v, u) \triangleq F_{hM} - F_{rM} + \mathcal{N}_{(1+\varepsilon)\mathcal{B}}(u) \tag{24e}$$
$$\Gamma_{+1a}(v, u) \triangleq \gamma_+(u; C_{hr}v, -C_{hb}\mathcal{S}(v - V_h)) \tag{24f}$$
$$\Gamma_{+1b}(v, u) \triangleq \gamma_+(u; C_{ph}v, -F_{rM} - C_{hb}\mathcal{S}(v - V_h)) \tag{24g}$$
$$\Gamma_{+2a}(v, u) \triangleq \gamma_+(u; C_{hr}v, F_{hP}) \tag{24h}$$
$$\Gamma_{+2b}(v, u) \triangleq \gamma_+(u; C_{ph}v, F_{hP} - F_{rM}) \tag{24i}$$
$$\Gamma_{+3a}(v, u) \triangleq \gamma_+(u; C_{tr}v, 0) \tag{24j}$$
$$\Gamma_{+3b}(v, u) \triangleq -F_{rM} + \mathcal{N}_{(1+\varepsilon)\mathcal{B}}(u) \tag{24k}$$
$$\Gamma_{-0a}(v, u) \triangleq \gamma_-(u; C_{th}v, -F_{rM}) \tag{24l}$$
$$\Gamma_{-0b}(v, u) \triangleq -F_{rM} + F_{hM} + \mathcal{N}_{(1+\varepsilon)\mathcal{B}}(u) \tag{24m}$$
$$\Gamma_{-1a}(v, u) \triangleq \gamma_-(u; C_{rh}v, -C_{rb}\mathcal{S}(v + V_r)) \tag{24n}$$
$$\Gamma_{-1b}(v, u) \triangleq \gamma_-(u; C_{pr}v, F_{hM} - C_{rb}\mathcal{S}(v + V_r)) \tag{24o}$$
$$\Gamma_{-2a}(v, u) \triangleq \gamma_-(u; C_{rh}v, -F_{rP}) \tag{24p}$$
$$\Gamma_{-2b}(v, u) \triangleq \gamma_-(u; C_{pr}v, -F_{rP} + F_{hM}) \tag{24q}$$
$$\Gamma_{-3a}(v, u) \triangleq \gamma_-(u; C_{th}v, 0) \tag{24r}$$
$$\Gamma_{-3b}(v, u) \triangleq F_{hM} + \mathcal{N}_{(1+\varepsilon)\mathcal{B}}(u). \tag{24s}$$

The constants appearing in (24) are defined as follows:

$$\begin{aligned} &C_{ph} \triangleq \sqrt{A_h^3/c_{ph}^2} \quad C_{tr} \triangleq \sqrt{A_r^3/c_{tr}^2} \\ &C_{th} \triangleq \sqrt{A_h^3/c_{th}^2} \quad C_{pr} \triangleq \sqrt{A_r^3/c_{pr}^2} \\ &C_{hr} \triangleq \sqrt{C_{ph}^2 + C_{tr}^2} \quad C_{rh} \triangleq \sqrt{C_{th}^2 + C_{pr}^2} \\ &C_{hb} \triangleq A_h^3/(c_b u_b)^2 \quad C_{rb} \triangleq A_r^3/(c_b u_b)^2 \\ &V_h \triangleq Q/A_h \quad V_r \triangleq Q/A_r \\ &F_{hP} \triangleq A_h P_M \quad F_{rP} \triangleq A_r P_M \\ &F_{hM} \triangleq A_h P_{hM} \quad F_{rM} \triangleq A_r P_{rM}. \end{aligned}$$

The graph of $f \in \Gamma(v, u)$ is illustrated in Fig. 2. As seen from Fig. 2(c), the function Γ is monotone with respect to the argument u and is single-valued when $v \neq 0$.

From tedious but straightforward derivation, one can see that the following lemma holds true:

Lemma 2: Let $f \in \overline{\mathbb{R}}$, $u \in (1+\varepsilon)\mathcal{B}$, $v_+ \in \mathbb{R}_+$, $v_- \in \mathbb{R}_-$, and $a \in \mathbb{R}$. Recall that the functions γ_+ and γ_- are defined as (23a) *and* (23b)*, respectively. Then, the following statements hold true*:

$$f \in \gamma_+(u; v_+, a) \iff u \in \theta_+(f; v_+, a) \tag{25}$$
$$f \in \gamma_-(u; v_-, a) \iff u \in \theta_-(f; v_-, a) \tag{26}$$

where the functions $\theta_+ : \overline{\mathbb{R}} \times \mathbb{R}_+ \times \mathbb{R} \rightrightarrows (1+\varepsilon)\mathcal{B}$ and $\theta_- : \overline{\mathbb{R}} \times \mathbb{R}_- \times \mathbb{R} \rightrightarrows (1+\varepsilon)\mathcal{B}$ are defined as follows:

$$\theta_+(f; \bar{v}, a) \triangleq \begin{cases} \dfrac{\bar{v}}{\max\left(\dfrac{\bar{v}}{1+\varepsilon}, \mathcal{R}(a - f)\right)} & \text{if } \bar{v} > 0 \\ \operatorname{gsgn}(0, f - a, 1 + \varepsilon) & \text{if } \bar{v} = 0 \end{cases} \tag{27a}$$

$$\theta_-(f; \bar{v}, a) \triangleq \begin{cases} \dfrac{-\bar{v}}{\min\left(\dfrac{\bar{v}}{1+\varepsilon}, \mathcal{R}(a - f)\right)} & \text{if } \bar{v} < 0 \\ \operatorname{gsgn}(-1 - \varepsilon, f - a, 0) & \text{if } \bar{v} = 0. \end{cases} \tag{27b}$$

Lemma 2 states that θ_+ and θ_- are the inverse functions of γ_+ and γ_- with respect to the first argument, respectively. Note that Γ in (24) is constructed from γ_+, γ_-, and $\mathcal{N}_{\mathcal{B}}$, and that the inverse function of $\mathcal{N}_{\mathcal{B}}$ is sgn from (7). Thus, one can see that the inverse function Θ of Γ can be derived from θ_+, θ_-, and sgn. Here, the fact that γ_+, γ_-, and $\mathcal{N}_{\mathcal{B}}$ are total, surjective, and monotone allows for the application of Lemmas 1 to obtain the analytical expression of $\Theta : \mathbb{R} \times \overline{\mathbb{R}} \rightrightarrows \mathcal{B}$ as follows:

$$\Theta(v, f) \triangleq \mathcal{B} \cap \operatorname{gsgn}(\Theta_-(v, f), v, \Theta_+(v, f)) \tag{28a}$$

where $\Theta_* : \mathbb{R} \times \overline{\mathbb{R}} \rightrightarrows (1+\varepsilon)\mathcal{B}$ are defined as follows:

$$\begin{aligned}\Theta_+(v, f) \triangleq \min\big(&\max\big(\min\left(\Theta_{+0a}(v, f), \Theta_{+0b}(v, f)\right),\\ &\min\left(\Theta_{+1a}(v, f), \Theta_{+1b}(v, f)\right), \min\left(\Theta_{+2a}(v, f),\right.\\ &\left.\Theta_{+2b}(v, f)\right)\big), \Theta_{+3a}(v, f), \Theta_{+3b}(v, f)\big)\end{aligned} \tag{28b}$$

$$\begin{aligned}\Theta_-(v, f) \triangleq \max\big(&\min\big(\max\left(\Theta_{-0a}(v, f), \Theta_{-0b}(v, f)\right),\\ &\max\left(\Theta_{-1a}(v, f), \Theta_{-1b}(v, f)\right), \max\left(\Theta_{-2a}(v, f),\right.\\ &\left.\Theta_{-2b}(v, f)\right)\big), \Theta_{-3a}(v, f), \Theta_{-3b}(v, f)\big)\end{aligned} \tag{28c}$$

and

$$\Theta_{+0a}(v, f) \triangleq \theta_+(f; C_{tr}v, F_{hM}) \tag{28d}$$
$$\Theta_{+0b}(v, f) \triangleq (1+\varepsilon)\operatorname{sgn}(f - F_{hM} + F_{rM}) \tag{28e}$$
$$\Theta_{+1a}(v, f) \triangleq \theta_+(f; C_{hr}v, -C_{hb}\mathcal{S}(v - V_h)) \tag{28f}$$
$$\Theta_{+1b}(v, f) \triangleq \theta_+(f; C_{ph}v, -F_{rM} - C_{hb}\mathcal{S}(v - V_h)) \tag{28g}$$
$$\Theta_{+2a}(v, f) \triangleq \theta_+(f; C_{hr}v, F_{hP}) \tag{28h}$$
$$\Theta_{+2b}(v, f) \triangleq \theta_+(f; C_{ph}v, F_{hP} - F_{rM}) \tag{28i}$$
$$\Theta_{+3a}(v, f) \triangleq \theta_+(f; C_{tr}v, 0) \tag{28j}$$
$$\Theta_{+3b}(v, f) \triangleq (1+\varepsilon)\operatorname{sgn}(f + F_{rM}) \tag{28k}$$
$$\Theta_{-0a}(v, f) \triangleq \theta_-(f; C_{th}v, -F_{rM}) \tag{28l}$$
$$\Theta_{-0b}(v, f) \triangleq (1+\varepsilon)\operatorname{sgn}(f - F_{hM} + F_{rM}) \tag{28m}$$
$$\Theta_{-1a}(v, f) \triangleq \theta_-(f; C_{rh}v, -C_{rb}\mathcal{S}(v + V_r)) \tag{28n}$$
$$\Theta_{-1b}(v, f) \triangleq \theta_-(f; C_{pr}v, F_{hM} - C_{rb}\mathcal{S}(v + V_r)) \tag{28o}$$
$$\Theta_{-2a}(v, f) \triangleq \theta_-(f; C_{rh}v, -F_{rP}) \tag{28p}$$
$$\Theta_{-2b}(v, f) \triangleq \theta_-(f; C_{pr}v, -F_{rP} + F_{hM}) \tag{28q}$$
$$\Theta_{-3a}(v, f) \triangleq \theta_-(f; C_{th}v, 0) \tag{28r}$$
$$\Theta_{-3b}(v, f) \triangleq (1+\varepsilon)\operatorname{sgn}(f - F_{hM}). \tag{28s}$$

Note that all Θ_* are total and surjective with respect to their second argument $f \in \overline{\mathbb{R}}$. The function Θ, however, is not total or surjective because the definition (28a) restricts its return value within $\mathcal{B}$, which means that it may be $\emptyset$ for some pairs of values of $v \in \mathbb{R}$ and $f \in \overline{\mathbb{R}}$.

B. SLIDING-MODE CONTROLLER FOR HYDRAULIC ACTUATORS

As has been mentioned in Section III-A, the function Θ defined in (28) is not convenient for the use in the controller because its output is not always a single value but can be a set or even the empty set. This section presents a single-valued total function Θ_s that is related to Θ through (22). A careful observation of the definition (24) of Γ and Fig. 2 reveals that the set-valuedness of $\Theta(v, f)$ takes place when f is at the maximum F_{hM} or the minimum $-F_{rM}$. When f is above F_{hM} or below $-F_{rM}$, $\Theta(v, f)$ is the empty set. In addition,

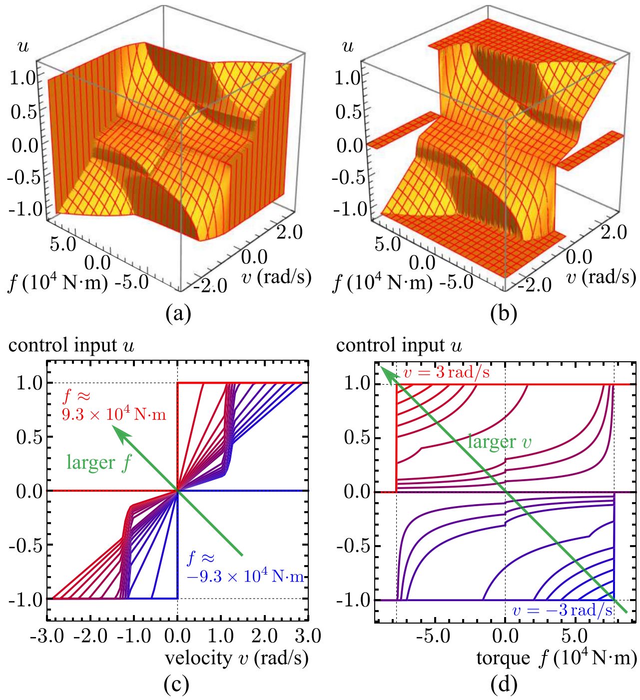

FIGURE 4. Inverse model of the actuator: (a) the graph of $f \in \Theta(v, f)$ defined in (21) and (b)(c)(d) the graph of $f = \Theta_S(v, f)$ defined in (32). The function Θ_S is obtained by removing the set-valuedness and non-totalness of the function Θ.

the definition (24a) implies that $\Theta(v, f)$ may be set-valued at $v = 0$. It may also be the case if $f = F_{hM} - F_{rM}$ because of the definitions (28e) and (28m) of $\Theta_{\pm 0b}$.

The use of an arbitrary single value within the set $\Theta(v, f)$ is justified in Theorem 1 in [15]. The theorem, however, depends on the assumption that the controller parameters are accurate with respect to the real actuator parameters. The system's sensitivity to the parametric errors may depend on the choice of the single value within the set. Through preliminary investigations, we propose the function Θ_s obtained by the following modifications of the definition (28) of Θ:

- Replace $\theta_\pm$ in (27) by

$$\theta_{+s}(f; \bar{v}, a) \triangleq \frac{\bar{v}}{\max\left(\bar{v}, \mathcal{R}(a - f)\right)} \tag{29a}$$
$$\theta_{-s}(f; \bar{v}, a) \triangleq \frac{-\bar{v}}{\min\left(\bar{v}, \mathcal{R}(a - f)\right)}. \tag{29b}$$

- Use $\Theta_{\pm *}$ ($* \in \{0a, 1a, 1b, 2a, 2b, 3a\}$) in (28d) to (28r) with $\theta_\pm$ being replaced by $\theta_{\pm s}$ in (29).
- Replace $\Theta_{\pm 0b}$ in (28e) and (28m) by

$$\Theta_{+0b,s}(v, f) \triangleq \begin{cases} 1 & \text{if } f \geq F_{hM} - F_{rM} \\ -1 & \text{if } f < F_{hM} - F_{rM} \end{cases} \tag{30a}$$
$$\Theta_{-0b,s}(v, f) \triangleq \begin{cases} 1 & \text{if } f > F_{hM} - F_{rM} \\ -1 & \text{if } f \leq F_{hM} - F_{rM}. \end{cases} \tag{30b}$$

- Replace $\Theta_{\pm 3b}$ in (28k), and (28s) by

$$\Theta_{+3b,s}(v,f) \triangleq \begin{cases} 1 & \text{if } f > -F_{rM} \\ 0 & \text{if } f \le -F_{rM} \end{cases} \tag{31a}$$

$$\Theta_{-3b,s}(v,f) \triangleq \begin{cases} 0 & \text{if } f \ge F_{hM} \\ -1 & \text{if } f < F_{hM}. \end{cases} \tag{31b}$$

- Use $\Theta_{\pm}$ in (28b) and (28c) as they are.
- Replace (28a) by

$$\Theta_s(v,f) \triangleq \begin{cases} \Theta_{-s}(v,f) & \text{if } v < 0 \\ 0 & \text{if } v = 0 \\ \Theta_{+s}(v,f) & \text{if } v > 0. \end{cases} \tag{32}$$

Note that the definitions (29) does not consider the case of $v = 0$ because (32) implies that $\Theta_{\pm}$ is not used when $v = 0$.

The original set-valued function Θ is illustrated in Fig. 4(a) while the derived singled-valued function Θ_s is shown in Figs. 4(b), (c) and (d). The motivation for this choice of the single-valued Θ_s is summarized as follows:

- Equation (29) is chosen so that $\theta_{\pm s}(f; \bar{v}, a) = \mathrm{sat}_{\mathcal{B}}(\theta_{\pm}(f; \bar{v}, a))$.
- Equation (30) is chosen to deal with the set-valuedness of $\Theta_{\pm 0b}$ that happens at $f = F_h - F_{rM}$. It is designed so that it allows $\Theta_{\pm 0a}(v,f)$ to be chosen in the min-max logic in (28b) and (28c). Nevertheless, $\Theta_{\pm 0b}$ are rarely in effect in the logic in (28b) and (28c) and actually have no effect in the numerical and experimental examples in this paper.
- Equation (31) is chosen to set $\Theta_s(v,f) = 0$ when $v > 0 \wedge f \le -F_{rM}$ or $v > 0 \wedge f \ge F_{rM}$ because, in these cases, the actuator needs to produce the maximally decelerating force and setting $u = 0$ (closing all main control valves) is the most robust way to realize it against the parametric errors.
- Equation (32) is chosen to set $\Theta_s(v,f) = 0$ when $v = 0$ because setting $u = 0$ (closing all main control valves) is the most robust way to achieve $v = 0$ against the parametric errors.

Employing the obtained function Θ_s in (32), we construct the algorithm to calculate the control input u as follows:

$$v_{f,k} := v_k + \hat{g}_k T/M_c \tag{33a}$$

$$v_{s,k} := (p_d - p_k)/(H + T) \tag{33b}$$

$$f_k := \mathrm{sat}_{\Gamma_s(T/M_c, v_{f,k}, \mathcal{B})}((v_{s,k} - v_{f,k})M_c/T) \tag{33c}$$

$$u_k := \Theta_s(v_{f,k} + f_k T/M_c, f_k) \tag{33d}$$

where M_c is the inertia of the controlled object and $\hat{g}_k$ is the estimated external force, which is set zero if unavailable. The singled-valued function Γ_s is the function satisfying (20). It can be implemented as

$$\Gamma_s(\eta, v, u) = (\Lambda(1/\eta, -v/\eta, u) - v)/\eta \tag{34}$$

where the function Λ is a function of which the complete analytical form is presented in [29]. Stability proofs for the controller (33) applied to the plant (16) are shown in Appendices B and C of [15].

The controller (33) depends on the inertia parameter M_c, which should be known in advance. When it is applied to the swing axis of an excavator, it should be the moment of inertia of the upperstructure. The upperstructure is composed of the cab and the links (the boom, arm, and bucket), which are combined with one another through components having some mechanical compliance. Therefore, it is not straightforward to judge whether M_c should be the moment of inertia of the whole upperstructure or only the cab part. The parameter M_c here is used to predict the actuator velocity $v_{f,k} + f_k T/M_c$ after the time T, which is 10 ms in our setup. Therefore, a suitable choice of M_c would depend on how far the effect of the actuator force is propagated within the time T within the structure. From some preliminary simulations and experiments, we conclude that it is better to set M_c as the moment of inertia only of the cab. Some supporting results will be presented in Sections IV and V.

C. STATE PREDICTOR FOR DEADTIME COMPENSATION

Hydraulic systems usually include the deadtime between the control input and the actuation. In order to compensate for the deadtime, the proposed controller includes a state predictor based on the quasistatic model [16] of the actuator.

To construct the predictor, we again consider the plant dynamics model (16). The implicit discretization of the model (16) is as follows:

$$v_{k+1} = v_k + (f_k + g_k)T/M \tag{35a}$$

$$p_{k+1} = p_k + v_{k+1}T \tag{35b}$$

$$f_k \in \Gamma(v_{k+1}, u_k). \tag{35c}$$

Eliminating v_{k+1} in (35c) and employing Γ_s in (34), we obtain the following expression:

$$f_k = \Gamma_s(T/M, v_k + g_k T/M, u_k) \tag{36a}$$

$$v_{k+1} = v_k + (f_k + g_k)T/M \tag{36b}$$

$$p_{k+1} = p_k + v_{k+1}T, \tag{36c}$$

which can be seen as the algorithm of a one-step predictor of the state $\{p_{k+1}, v_{k+1}\}$ based on the inputs $\{p_k, v_k, u_k, g_k\}$.

By iteratively using the one-step predictor (36), we can construct the algorithm of a multi-step predictor for a look-ahead time $\hat{T}_d$ as follows:

for $i \leftarrow 1$ **to** $\mathrm{floor}(\hat{T}_d/T) - 1$ **do**

$$U[i+1] \leftarrow U[i] \tag{37a}$$

end for

$$U[1] \leftarrow u \tag{37b}$$

for $i \leftarrow \mathrm{floor}(\hat{T}_d/T)$ **to** 1 **do**

$$f \leftarrow \Gamma_s(T/M_p, v + \hat{g}T/M_p, U[i]) \tag{37c}$$

$$v \leftarrow v + (f + \hat{g})T/M_p \tag{37d}$$

$$p \leftarrow p + vT \tag{37e}$$

end for

return p **and** v

where floor means the maximum integer that does not exceed the argument, M_p is the inertia of the controlled object, and $\hat{g}$ is the estimated external force. Here, $U[i]$ ($i \in \{1, \cdots, \text{floor}(\hat{T}_d/T)\}$) is the buffer to store the control inputs u of i timesteps ago. As has been illustrated in Fig. 3, the finally obtained p and v are provided to the sliding-mode controller (33) as the inputs.

The predictor (37) also depends on the prior knowledge of the inertia M_p of the controlled object, as is the case with the controller (33). When it is applied to the swing axis of an excavator, we again need to consider that the moment of inertia of which part of the upperstructure should be used as M_p. The predictor (37) is for predicting the time $\hat{T}_d$ later, in our setup, it is about 150 to 450 ms, which is 15 to 45 times of T. Considering that the effect of the actuator force in the upperstructure is propagated further in $\hat{T}_d$ than in T, we can see that the moment of inertia M_p for the predictor (37) should be larger than the moment of inertia M_c for the controller (33). Our conclusion from some preliminary simulations and experiments is that it is better to set M_p as the moment of inertia of the whole upperstructure. Supporting results will be shown in Sections IV and V.

IV. SIMULATIONS

A. SIMULATION SETUP

The proposed controller, which is the sliding-mode controller (33) combined with the state predictor (37), was validated with our realtime simulator [30] of a 20-ton class hydraulic excavator. The controller was constructed with MATLAB/Simulink and the simulator is constructed with Microsoft Visual C++. They are connected as illustrated in Fig. 5 through TCP/IP sockets at the cycle of 10 ms, i.e., the controller's sampling interval is $T = 10$ ms. The simulator's timestep size is 0.1 ms. The proposed controller was tested with the angle p of the swing axis, driven by a rotary hydraulic actuator, of the simulated excavator. In the simulations, the desired angle p_d and the parameter H were fixed as 90° and 1.5 s, respectively. The estimated external force $\hat{g}$ was set as 0 because the excavator was placed horizontally.

The simulator deals with links as rigid bodies connected by virtual viscoelastic elements through virtual beams as illustrated in the green circle in Fig. 6. The stiffness and the viscosity of the virtual viscoelastic elements are 5.0×10^7 N/m and 3.0×10^5 N·s/m, respectively, and the length of the virtual beams is 2.0 m. The frictions in the joints are implemented by the technique presented in [31].

In the simulator, the torque of the rotary hydraulic actuator is calculated based on the nonsmooth quasistatic model explained in Section II-B. The parameters of the actuator are shown in Table 1. The torque is amplified by a geared transmission with the reduction ratio 130. The output shaft of the actuator is connected to the cab through a virtual torsional viscoelastic element with the stiffness 5.0×10^7 N·m/rad and the viscosity 3.0×10^5 N·m·s/rad as illustrated in the blue circle in Fig. 6, employing the technique presented in [29].

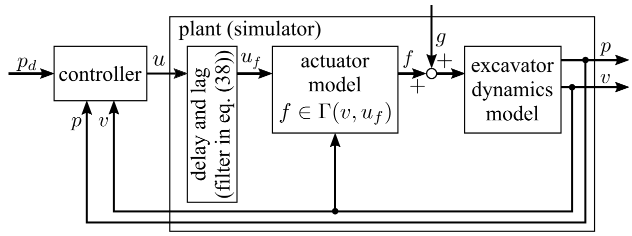

FIGURE 5. Simulation setup.

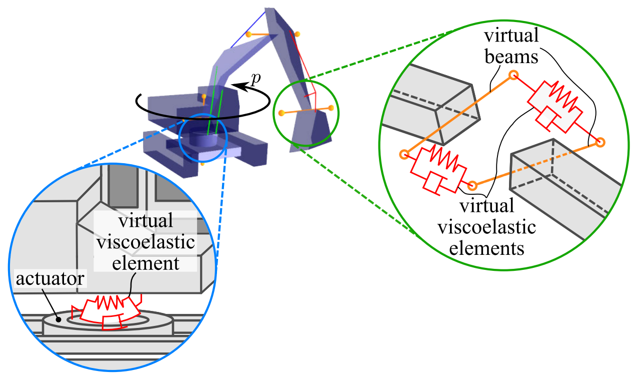

FIGURE 6. Connections of links in the simulator: the figure in the green circle illustrates the connections among links through the virtual viscoelastic elements and the virtual beams, and the figure in the blue circle illustrates the connection between the cab and the rotary actuator.

TABLE 1. Parameters of the rotary hydraulic actuator in the simulations.

symbols	physical meanings	values and units
V	chamber volume of the rotary actuator	129×10^{-6} m^3
A_h, A_r	equivalent cross-sectional areas of the chambers ($V/(2\pi)$)	2.05×10^{-5} m^3
P_{hM}, P_{rM}	pressure limit of the relief valves	29 MPa
P_M	pressure limit of the pump relief valve	35 MPa
Q	oil supply flowrate from the pump	3.7×10^{-3} m^3/s
a_{ph}, a_{pr}	max opening area of the main control valves connected to the pump	1.2×10^{-4} m^2
a_{tr}, a_{th}	max opening area of the main control valves connected to the tank	5.0×10^{-5} m^2
a_b	max opening area of the bleed valve	1.0×10^{-4} m^2
u_b	ratio of the bleed valve opening area	0.1
$C_{ph}, C_{pr}, C_{tr}, C_{th}, C_b$	discharge coefficients	0.6
ρ	mass density of the oil	850 kg/m^3

The rotary hydraulic actuator accepts the control input u of the deadtime T_d ago. In addition, the responses of the main control valves are assumed to be lagged by the dynamics of the spool valves. In order to emulate the delay and the lag, we include the following filter between the controller and the actuator as shown in Fig. 5:

$$u_f = \mathcal{L}^{-1}\left[\frac{\omega_0^2 e^{-T_d s}\mathcal{L}[u]}{s^2 + 2\zeta\omega_0 s + \omega_0^2}\right] \tag{38}$$

where $\mathcal{L}$ represents the Laplace transform. The deadtime T_d, the cutoff frequency ω_0, and the damping ratio ζ are set as 300 ms, 94.2 ($\approx 30\pi$) rad/s, and 1, respectively.

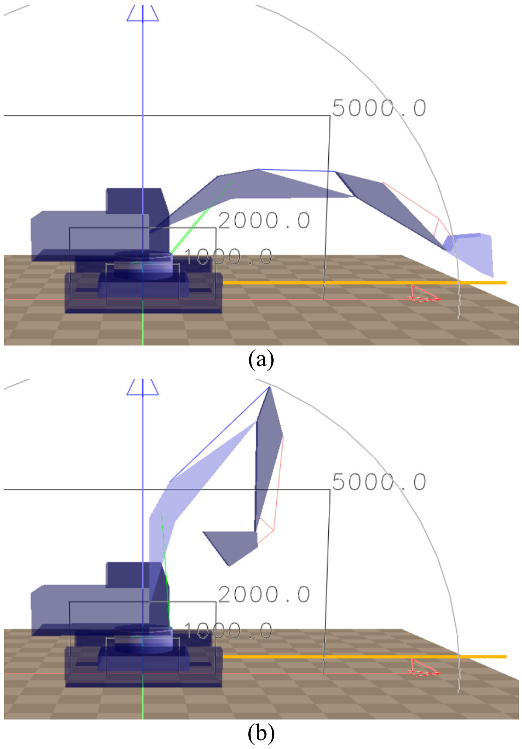

FIGURE 7. Configurations of the excavator in the simulation: (a) the extended configuration and (b) the flexed configuration.

The simulations were performed in two different configurations illustrated in Fig. 7, which are the extended configuration and the flexed configuration. In the extended configuration, the moment of inertia of the whole upperstructure, which is composed of the cab, the boom, the arm, and the bucket, is $J_{\mathrm{up,ex}} \triangleq 1.34 \times 10^5$ kg·m^2. In the flexed configuration, it is $J_{\mathrm{up,fl}} \triangleq 5.66 \times 10^4$ kg·m^2. The moment of inertia of only the cab is $J_{\mathrm{cab}} \triangleq 3.37 \times 10^4$ kg·m^2.

Other position controllers were not compared in the simulations. The main feature of the proposed controller is that it explicitly intends to realize specified transient behaviors in set-point control tasks with only a few adjustable controller parameters. Other controllers, such as PID-based controllers [7]–[10] and sliding-mode controllers [1], [5], [6] may realize similar behaviors, but it would require careful parameter tuning and careful design of the target trajectory. Thus, we leave empirical comparisons outside the scope of this paper.

B. EFFECTS OF SETTINGS OF INERTIA PARAMETERS AND DEADTIME

Some simulations were performed to check the effects of the inertia parameters $\{M_c, M_p\}$ and the predictor and the look-ahead time $\hat{T}_d$. We performed the simulations with the following three settings of the inertia parameters $\{M_c, M_p\}$:

- Setting A: $M_c = M_p = J_{\mathrm{cab}}$.
- Setting B: $M_c = J_{\mathrm{cab}}$ and $M_p = J_{\mathrm{up},*}$.
- Setting C: $M_c = M_p = J_{\mathrm{up},*}$.

The look-ahead time $\hat{T}_d$ was set as seven different values from 150 ms to 450 ms. The actuator-model parameters in the controller were set idealistically, being equal to the plant parameter values in Table 1. It should be noted that the second-order lag (38) in the plant is not taken into consideration in the controller.

Fig. 8 shows simulation results in the extended configuration. It shows that the swing angle p converges to the desired angle p_d in all settings. From the comparison among different settings of the inertia parameters, one can see that Setting B is the most suitable because it results in the control input u being non-oscillatory and the state $\{p, v\}$ being closest to the switching surface $\sigma = 0$. This result is consistent with the discussions in Sections III-B and III-C, i.e., M_c should be the moment of inertia of the cab and M_p should be that of the whole upperstructure. The chattering-like behavior in u of Setting C can be explained as that an excessively large value of M_c results in an unnecessarily large value of f_k in (33c), leading to a saturated value of u. From the comparison among the different $\hat{T}_d$ values, one can see that setting the accurate value to $\hat{T}_d$ results in accurate sliding on the switching surface.

Fig. 9 shows simulation results in the flexed configuration. Also in this configuration, the swing angle p converges to the desired angle p_d in all parameter settings. It is also apparent that the three settings of the inertia parameters do not cause much difference, resulting in non-oscillatory input u and reasonably accurate sliding on the switching surface $\sigma = 0$. It can be attributed to the fact that the ratio $J_{\mathrm{up,fl}}/J_{\mathrm{cab}} = 1.68$ in the flexed configuration is much smaller than $J_{\mathrm{up,ex}}/J_{\mathrm{cab}} = 3.98$ in the extended configuration. One can also see that $\hat{T}_d$ closer to T_d results in the state trajectory closer to the switching surface, as was the case with the extended configuration.

In Figs. 8 and 9, one can see that at least one of the chamber pressures P_h and P_r was always saturated, which means that the effects of the relief valves cannot be neglected in situations like these simulations. These results show that the controller appropriately constrains the state to the switching surface $\sigma = 0$ even during these saturated periods, exhibiting the benefit of the controller accounting for the strong nonlinearity caused by the valve behaviors.

It should be noted that the speed of convergence is determined by the parameter H and it can be made faster by setting H smaller. The value of H, however, should not be set too small because it can result in overshoots, i.e., penetration of the state through the switching surface. Appendix B of [15] details the conditions for the state constrained to the switching surface. Different types of switching surfaces, such as those nonlinear, may be effective to make the convergence faster without producing overshoots, but it is left outside the scope of this paper.

C. EFFECTS OF MODELING ERRORS

Another set of simulations was conducted to test the influence of the parametric errors in the actuator model. For

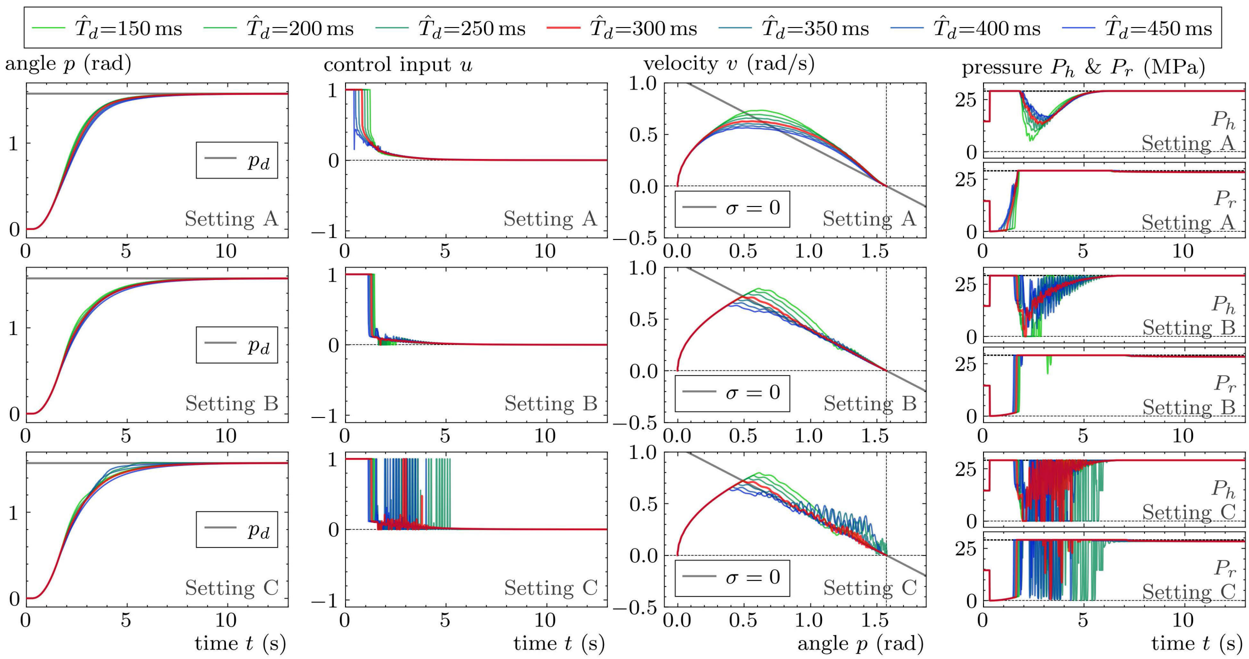

FIGURE 8. Simulation results in the extended configuration with three different settings of the inertia parameters $\{M_c, M_p\}$ and different values of the look-ahead time $\hat{T}_d$. Settings A, B, and C stand for $\{M_c, M_p\} = \{J_{\mathrm{cab}}, J_{\mathrm{cab}}\}$, $\{J_{\mathrm{cab}}, J_{\mathrm{up,ex}}\}$, and $\{J_{\mathrm{up,ex}}, J_{\mathrm{up,ex}}\}$, respectively. The red curves represent results with $\hat{T}_d = T_d$. The result of Setting B with $\hat{T}_d = 300$ ms can be seen as the most suited among those presented here.

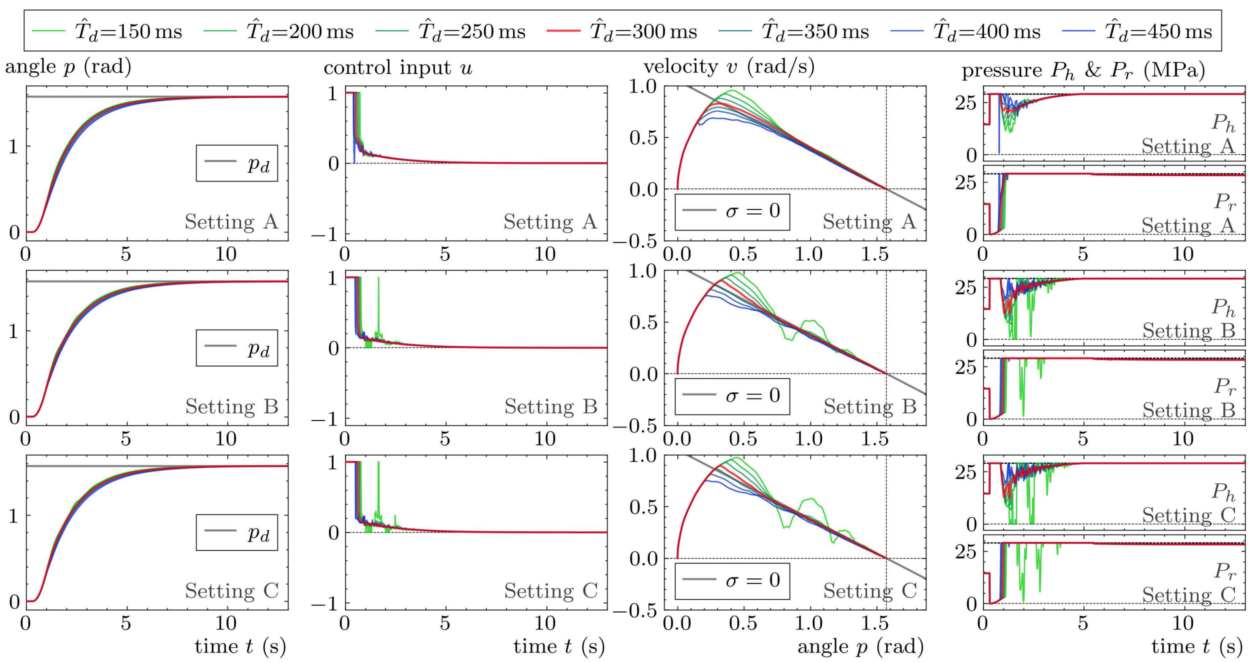

FIGURE 9. Simulation results in the flexed configuration with three different settings of the inertia parameters $\{M_c, M_p\}$ and different values of the look-ahead time $\hat{T}_d$. Settings A, B, and C stand for $\{M_c, M_p\} = \{J_{\mathrm{cab}}, J_{\mathrm{cab}}\}$, $\{J_{\mathrm{cab}}, J_{\mathrm{up,fl}}\}$, and $\{J_{\mathrm{up,fl}}, J_{\mathrm{up,fl}}\}$, respectively. The red curves represent results with $\hat{T}_d = T_d$.

each configuration, 100 trials were performed with all parameters listed in Table 1 being randomly varied by −15%, 0%, or 15%. The inertia parameters were set as $M_c = J_{\mathrm{cab}}$ and $M_p = J_{\mathrm{up},*}$, i.e., Setting B. The look-ahead time $\hat{T}_d$ was fixed to 300 ms, i.e., the true deadtime T_d.

Fig. 10 shows the results. In all parameter settings, the angle p converges to the desired angle p_d, although some settings result in chattering-like behaviors in u and separation of the state from the switching surface $\sigma = 0$. These results exhibit a certain robustness of the proposed controller against the modeling errors.

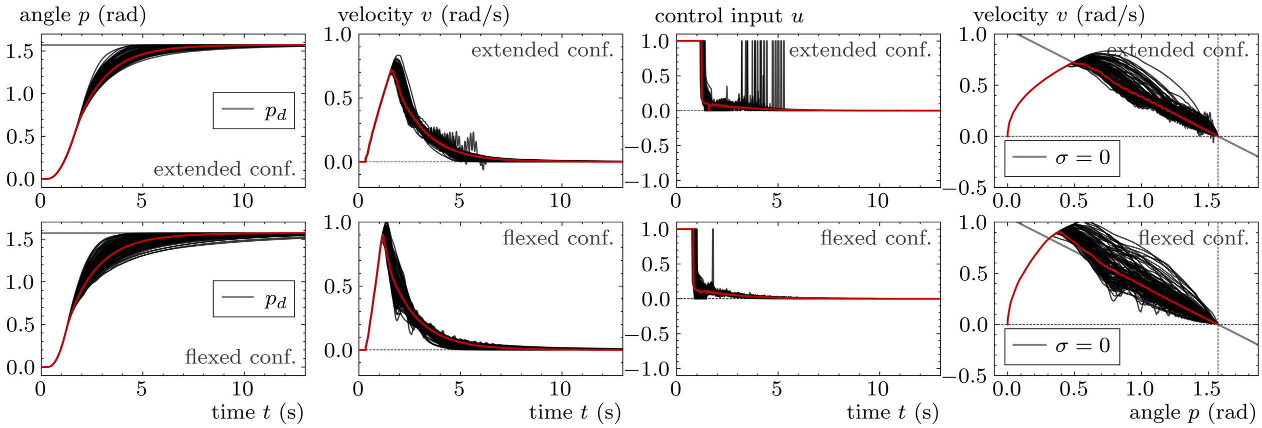

FIGURE 10. Simulation results with modeling errors that are randomly selected in $\{-15\,\%, 0\%, +15\,\%\}$ for each parameter listed in Table 1. The red line shows an almost ideal case with no modeling errors. The number of trials is 100 for each configuration. The inertia parameters are set as $\{M_c, M_p\} = \{J_{\mathrm{cab}}, J_{\mathrm{up},*}\}$, i.e., Setting B. The look-ahead time $\hat{T}_d$ is 300 ms ($=T_d$).

V. EXPERIMENTS

A. EXPERIMENT SETUP

We tested the proposed controller with a 13-ton class excavator, Kobelco ED160-5 (with its dozer blade removed), shown in Fig. 11. The controller was applied to the angle p of the swing axis driven by a rotary hydraulic actuator, which has a structure similar to the one shown in Fig. 1. In the circuit, a single four-port spool valve plays the role of four main control valves. The spool valve is driven by a pair of electromagnetic control valves that accept the control input u so that the spool displacement is proportional to the control input u. Further detailed specifications of the actuator and the excavator are not reported here due to proprietary restrictions.

(a)

(b)

FIGURE 11. Kobelco 13-ton class excavator in the extended configuration (a) and in the flexed configuration (b).

The controller was constructed with MATLAB/Simulink. It was connected with the excavator through the Control Area Network (CAN) to receive the sensor reading of the angular velocity v, which was measured by a microelectromechanical systems (MEMS) gyroscope, and send the control input u to the spool valve at the sampling interval of $T = 10$ ms. The angle p was obtained by simply integrating the measured angular velocity v, being reset at the beginning of every trial. The internal pressures of the chambers, unfortunately, could not be obtained for some hardware reasons. The desired angle p_d and the controller parameter H were fixed at 90° and 1.5 s, respectively, as was the case with the simulations in Section IV. The estimated external force $\hat{g}$ was set as 0 because the excavator was placed horizontally. We used three different settings for the inertia parameters $\{M_c, M_p\}$, which were Settings A, B, and C introduced in Section IV-B. The values of $J_{\mathrm{up,ex}}$, $J_{\mathrm{up,fl}}$, and J_{cab} (cf. Section IV-A for definitions) were obtained from the nominal specifications of the excavators, of which the ratios were $J_{\mathrm{up,ex}}/J_{\mathrm{cab}} = 9.92$ and $J_{\mathrm{up,fl}}/J_{\mathrm{cab}} = 4.61$. Because the deadtime T_d was not accurately available, the look-ahead time $\hat{T}_d$ was tested at five different values, which were 0 ms (i.e., without the state predictor), 300 ms, 400 ms, 500 ms, and 600 ms.

We did not test other controllers in the experiments for the same reasons as in the simulations in Section IV. Another reason, more practical, was that the behavior of simple linear controllers would be quite unpredictable, especially in the early stage of parameter tuning, posing difficulty in ensuring safety.

B. RESULTS

Fig. 12 shows results in the extended configuration. It shows that the swing angle p converges to the desired angle p_d except the case without the deadtime compensation. It can be seen that Setting B is more suitable than Settings A and C because the state trajectory is the closest to the switching

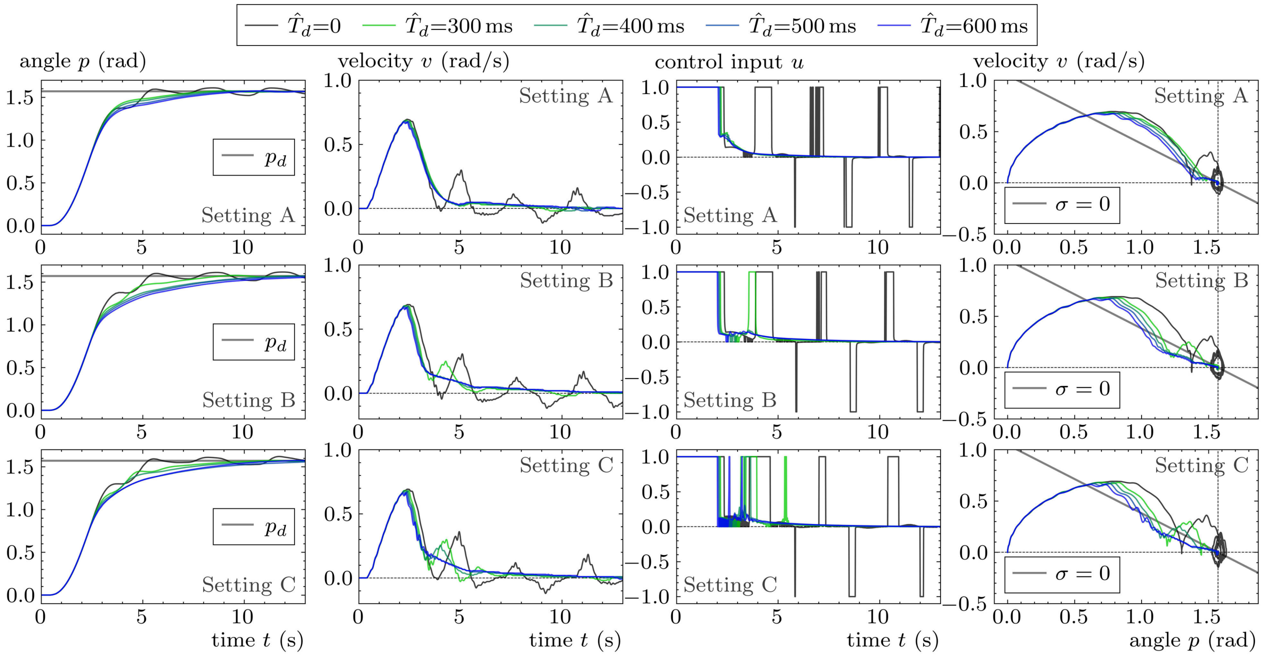

FIGURE 12. Experiments in the extended configuration with three different settings of the inertia parameters $\{M_c, M_p\}$ and different values of the look-ahead time $\hat{T}_d$. Settings A, B, and C stand for $\{M_c, M_p\} = \{J_{\text{cab}}, J_{\text{cab}}\}$, $\{J_{\text{cab}}, J_{\text{up,ex}}\}$, and $\{J_{\text{up,ex}}, J_{\text{up,ex}}\}$, respectively.

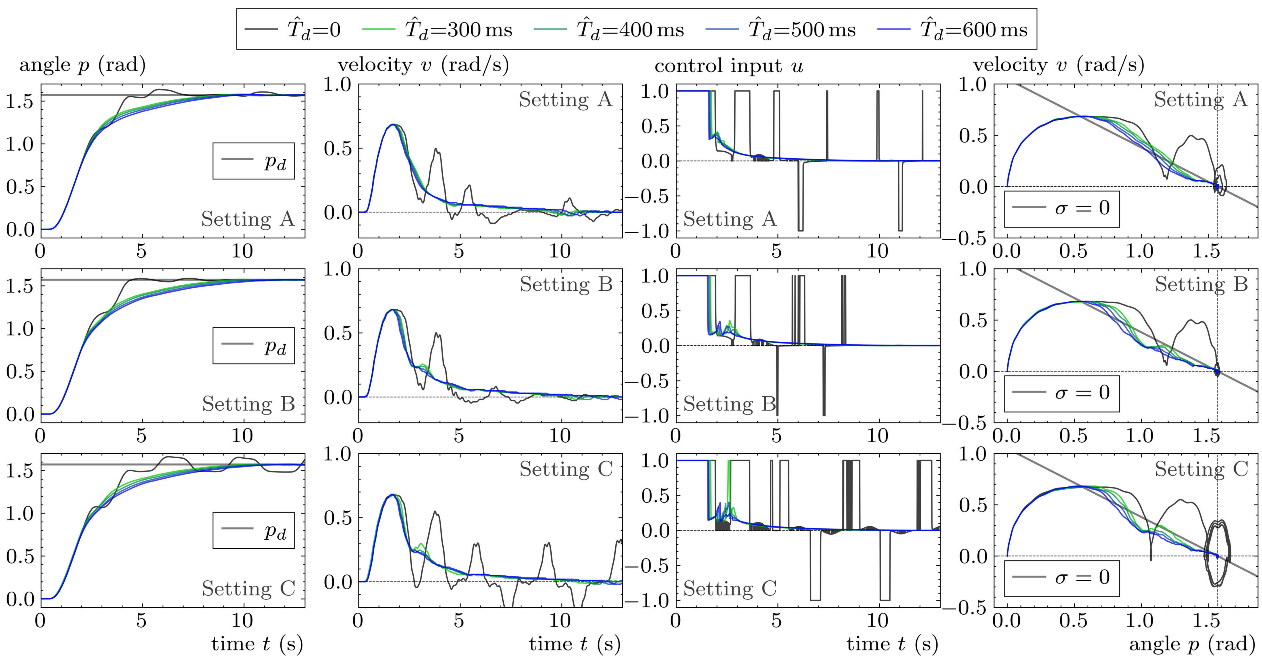

FIGURE 13. Experiments in the flexed configuration with three different settings of the inertia parameters $\{M_c, M_p\}$ and different values of the look-ahead time $\hat{T}_d$. Settings A, B, and C stand for $\{M_c, M_p\} = \{J_{\text{cab}}, J_{\text{cab}}\}$, $\{J_{\text{cab}}, J_{\text{up,fl}}\}$, and $\{J_{\text{up,fl}}, J_{\text{up,fl}}\}$, respectively.

surface $\sigma = 0$ and the chattering of the control input u is smaller. One can see the importance of the chattering reduction by observing the fluctuation in the velocity v coinciding with the chattering in u. From the comparison among the different $\hat{T}_d$ values, one can see that it is safer to set $\hat{T}_d$ larger, especially larger than 400 ms in this setup, to avoid undesirable artifacts. For example, the undesirable velocity fluctuation seen in $t \in [3\text{ s}, 5\text{ s}]$ with $\hat{T}_d = 300$ ms is suppressed with larger values of $\hat{T}_d$. Even larger $\hat{T}_d$ were not tested in the experiments, but it would be natural to assume that the range of suitable values of the look-ahead time $\hat{T}_d$ are upperbounded by the accuracy of the state predictor.

Fig. 13 shows results in the flexed configuration. It shows that the swing angle p converges to the desired angle p_d also in this configuration, as long as the state predictor is used. It can be seen that the setting of the inertia parameters does not largely affect the results in this configuration, similarly to the simulations in Section IV-B, presumably because the ratio $J_{\mathrm{up,fl}}/J_{\mathrm{cab}}$ was relatively closer to one. It can also be seen that rather acceptable behavior was realized as long as the look-ahead time $\hat{T}_d$ was between 300 ms to 600 ms.

In both configurations with all settings, the state trajectory penetrated the switching surface. It can be attributed to the inaccuracy of the state predictor, which currently does not consider the dynamics of the spool valve or the pressure dynamics (i.e., the compressibility) of the oil. We do not practically consider it as a primary concern because it does not result in overshooting in the angle or abrupt changes in the velocity. It may however be worth investigating to improve the state predictor by including unmodeled dynamics by extending the quasistatic model [16] of the actuator.

VI. CONCLUSION

This paper has proposed a sliding-mode set-point position controller for hydraulic excavators that realizes appropriate converging behavior to the desired position. The proposed controller consists of a sliding-mode controller constructed with a double-implicit implementation scheme [15] and a state predictor based on a nonsmooth quasistatic model [16] of the hydraulic actuator. The controller has been validated through simulations and experiments, in which the swing angle converged to the desired angle with an appropriate transient behavior along the sliding surface. The effects of the controller's parameters, especially the inertia parameters and the look-ahead time, have also been investigated in the simulations and the experiments.

Future work should address extending the proposed controller to a multi-DOF controller that simultaneously deals with all actuators (the boom, arm, and bucket cylinders). In many commercial excavators, a single pump drives more than one actuator, and thus the motion of an actuator often affects the motion of another actuator. Such effects would need to be taken into account in multi-DOF position control, for which the model presented in Section II-B of [16] would be useful. Moreover, for enhancing the efficiency of positioning and trajectory-tracking tasks, different types of switching surfaces may need to be employed. A previous theoretical study [15] suggests that a steeper switching surface realizes faster convergence but fails to maintain the sliding mode in a high-velocity region. It is thus logical to consider that a faster convergence would be realized by a nonlinear switching surface whose slope is steeper in a lower-velocity region. Therefore, switching surfaces with saturated velocity [32] and a square-root-like nonlinearity [33] would be worth investigating.

APPENDIX A
PROOF OF LEMMA 1

To provide the proof of Lemma 1, let us define the following operators:

$$_{\geq\exists}\mathcal{X} \triangleq \{\xi \in \overline{\mathbb{R}} \mid \xi \geq \exists x \in \mathcal{X}\} \tag{39a}$$
$$_{\leq\exists}\mathcal{X} \triangleq \{\xi \in \overline{\mathbb{R}} \mid \xi \leq \exists x \in \mathcal{X}\} \tag{39b}$$

where $\mathcal{X} \subset \overline{\mathbb{R}}$. With these operators, we have the following lemma:

Lemma 3: Let $f : \mathcal{C} \rightrightarrows \overline{\mathbb{R}}$ be a total, surjective, monotone, set-valued function where $\mathcal{C} \subset \overline{\mathbb{R}}$. Then, $y \in {}_{\geq\exists}f(x) \iff x \in {}_{\leq\exists}f^{-1}(y)$ and $y \in {}_{\leq\exists}f(x) \iff x \in {}_{\geq\exists}f^{-1}(y)$ are satisfied.

Proof: The first statement can be proven as follows:

$$\begin{aligned}
y \in {}_{\geq\exists}f(x) &\iff \exists y_0 \text{ s.t. } f(x) \ni y_0 \leq y \\
&\iff \exists y_0, x_1 \text{ s.t. } f(x) \ni y_0 \leq y \in f(x_1) \\
&\qquad (\because \text{surjectivity of } f) \\
&\iff \exists y_0, x_1 \text{ s.t. } f^{-1}(y_0) \ni x \leq x_0 \in f^{-1}(y) \\
&\qquad (\because \text{monotonicity of } f) \\
&\iff \exists x_1 \text{ s.t. } x \leq x_1 \in f^{-1}(y) \\
&\qquad (\because \text{surjectivity of } f^{-1}) \\
&\iff x \in {}_{\leq\exists}f^{-1}(y).
\end{aligned} \tag{40}$$

The second statement can also be proven in the same manner. □

The definitions (12) of the min and max operators can be equivalently rewritten as follows:

$$\max(\mathcal{X}, \mathcal{Y}) \triangleq (\mathcal{X} \cap {}_{\geq\exists}\mathcal{Y}) \cup ({}_{\geq\exists}\mathcal{X} \cap \mathcal{Y}) \tag{41a}$$
$$\min(\mathcal{X}, \mathcal{Y}) \triangleq (\mathcal{X} \cap {}_{\leq\exists}\mathcal{Y}) \cup ({}_{\leq\exists}\mathcal{X} \cap \mathcal{Y}) \tag{41b}$$

where $\mathcal{X} \subset \overline{\mathbb{R}}$ and $\mathcal{Y} \subset \overline{\mathbb{R}}$. Now we are in position to provide the proof of Lemma 1.

Proof of Lemma 1: If $f(x) \triangleq \min(f_1(x), f_2(x))$, one has the following:

$$\begin{aligned}
y \in f(x) &\iff \big(y \in f_1(x) \wedge y \in {}_{\geq\exists}f_2(x)\big) \\
&\qquad \vee \big(y \in {}_{\geq\exists}f_1(x) \wedge y \in f_2(x)\big) \\
&\iff \Big(x \in f_1^{-1}(y) \wedge x \in {}_{\leq\exists}f_2^{-1}(x)\Big) \\
&\qquad \vee \Big(x \in {}_{\leq\exists}f_1^{-1}(y) \wedge x \in f_2^{-1}(y)\Big) \\
&\iff x \in \max(f_1^{-1}(y), f_2^{-1}(y)).
\end{aligned} \tag{42}$$

The first and second lines of the above are connected by Lemma 3. The case of $f(x) \triangleq \max(f_1(x), f_2(x))$ can also be proven in the same manner. □

REFERENCES

[1] J. Kim, M. Jin, W. Choi, and J. Lee, "Discrete time delay control for hydraulic excavator motion control with terminal sliding mode control," *Mechatronics*, vol. 60, pp. 15–25, Jun. 2019, doi: 10.1016/j.mechatronics.2019.04.008.

[2] P. H. Chang and S.-J. Lee, "A straight-line motion tracking control of hydraulic excavator system," *Mechatronics*, vol. 12, no. 1, pp. 119–138, Feb. 2002, doi: 10.1016/S0957-4158(01)00014-9.

[3] Y. Wang, L. Gu, B. Chen, and H. Wu, "A new discrete time delay control of hydraulic manipulators," *Proc. Inst. Mech. Eng. I, J. Syst. Control Eng.*, vol. 231, no. 3, pp. 168–177, Mar. 2017, doi: 10.1177/0959651816689340.
[4] Y. Li and Q. Wang, "Adaptive neural finite-time trajectory tracking control of hydraulic excavators," *Proc. Inst. Mech. Eng. I, J. Syst. Control Eng.*, vol. 232, no. 7, pp. 909–925, 2018, doi: 10.1177/0959651818767770.
[5] J. Xu and H.-S. Yoon, "Sliding mode control of hydraulic excavator for automated grading operation," *SAE Int. J. Commertial Veh.*, vol. 11, no. 2, pp. 113–123, 2018, doi: 10.4271/02-11-02-0010.
[6] L. Schmidt, T. O. Andersen, and H. C. Pedersen, "Finite-time convergent continuous control design based on sliding mode algorithms with application to a hydraulic drive," *Int. J. Mechatronics Autom.*, vol. 4, no. 3, pp. 188–199, 2014, doi: 10.1504/IJMA.2014.064100.
[7] B. M Brentan, E. Luvizotto, Jr., I. Montalvo, J. Izquierdo, and R. Pérez-García, "Position control of nonlinear hydraulic system using an improved PSO based PID controller," *Mech. Syst. Signal Process.*, vol. 83, no. 15, pp. 241–259, 2017, doi: 10.1016/j.ymssp.2016.06.010.
[8] H. Feng, W. Ma, C. Yin, and D. Cao, "Trajectory control of electro-hydraulic position servo system using improved PSO-PID controller," *Autom. Construct.*, vol. 127, Jul. 2021, Art. no. 103722, doi: 10.1016/j.autcon.2021.103722.
[9] H. Feng, C. B. Yin, W. Weng, W. Ma, J. Zhou, and W. Jia, "Robotic excavator trajectory control using an improved GA based PID controller," *Mech. Syst. Signal Process.*, vol. 105, pp. 153–168, May 2018, doi: 10.1016/j.ymssp.2017.12.014.
[10] H. Feng, C. Yin, W. Ma, H. Yu, and D. Cao, "Parameters identification and trajectory control for a hydraulic system," *ISA Trans.*, vol. 92, pp. 228–240, Sep. 2019, doi: 10.1016/j.isatra.2019.02.022.
[11] S. Kim, J. Park, S. Kang, P. Y. Kim, and H. J. Kim, "A robust control approach for hydraulic excavators using μ-synthesis," *Int. J. Control, Autom. Syst.*, vol. 16, no. 4, pp. 1615–1628, 2018, doi: 10.1007/s12555-017-0071-9.
[12] W. Borutzky, B. Barnard, and J. Thoma, "An orifice flow model for laminar and turbulent conditions," *Simul. Model. Pract. Theory*, vol. 10, no. 3, pp. 141–152, 2002, doi: 10.1016/S1569-190X(02)00092-8.
[13] R. Kikuuwe, S. Yasukouchi, H. Fujimoto, and M. Yamamoto, "Proxy-based sliding mode control: A safer extension of PID position control," *IEEE Trans. Robot.*, vol. 26, no. 4, pp. 670–683, Aug. 2010, doi: 10.1109/TRO.2010.2051188.
[14] R. Kikuuwe, "Sliding motion accuracy of proxy-based sliding mode control subjected to measurement noise and disturbance," *Eur. J. Control*, vol. 58, pp. 114–122, Mar. 2021, doi: 10.1016/j.ejcon.2020.07.005.
[15] R. Kikuuwe, Y. Yamamoto, and B. Brogliato. (2021). *Implicit Implementation of Nonsmooth Controllers to Nonsmooth Actuators*. [Online]. Available: https://hal.inria.fr/hal-03180790
[16] R. Kikuuwe, T. Okada, H. Yoshihara, T. Doi, T. Nanjo, and K. Yamashita, "A nonsmooth quasi-static modeling approach for hydraulic actuators," *J. Dyn. Syst., Meas., Control*, vol. 143, no. 12, Dec. 2021, Art. no. 121002, doi: 10.1115/1.4051894.
[17] J. Shi, L. Quan, X. Zhang, and X. Xiong, "Electro-hydraulic velocity and position control based on independent metering valve control in mobile construction equipment," *Autom. Construct.*, vol. 94, pp. 73–84, Oct. 2018, doi: 10.1016/j.autcon.2018.06.005.
[18] X. Zhang, S. Qiao, L. Quan, and L. Ge, "Velocity and position hybrid control for excavator boom based on independent metering system," *IEEE Access*, vol. 7, pp. 71999–72011, 2019, doi: 10.1109/ACCESS.2019.2919953.
[19] D. Cristofori and A. Vacca, "Modeling hydraulic actuator mechanical dynamics from pressure measured at control valve ports," *Proc. Inst. Mech. Eng., I, J. Syst. Control Eng.*, vol. 229, no. 6, pp. 541–558, Jul. 2015, doi: 10.1177/0959651814568366.
[20] A. Lichtarowicz, R. K. Duggins, and E. Markland, "Discharge coefficients for incompressible non-cavitating flow through long orifices," *J. Mech. Eng. Sci.*, vol. 7, no. 2, pp. 210–219, 1965. [Online]. Available: https://journals.sagepub.com/doi/10.1243/JMES_JOUR_1965_007_029_02, doi: 10.1243/JMES_JOUR_1965_007_029_02.
[21] Y. Ye, C.-B. Yin, X.-D. Li, W.-J. Zhou, and F.-F. Yuan, "Effects of groove shape of notch on the flow characteristics of spool valve," *Energy Convers. Manage.*, vol. 86, pp. 1091–1101, Oct. 2014, doi: 10.1016/j.enconman.2014.06.081.
[22] D. Wu, R. Burton, and G. Schoenau, "An empirical discharge coefficient model for orifice flow," *Int. J. Fluid Power*, vol. 3, no. 3, pp. 13–19, Jan. 2002, doi: 10.1080/14399776.2002.10781143.
[23] O. Huber, V. Acary, B. Brogliato, and F. Plestan, "Implicit discrete-time twisting controller without numerical chattering: Analysis and experimental results," *Control Eng. Pract.*, vol. 46, pp. 129–141, Jan. 2016, doi: 10.1016/j.conengprac.2015.10.013.
[24] B. Wang, B. Brogliato, V. Acary, A. Boubakir, and F. Plestan, "Experimental comparisons between implicit and explicit implementations of discrete-time sliding mode controllers: Toward input and output chattering suppression," *IEEE Trans. Control Syst. Technol.*, vol. 23, no. 5, pp. 2071–2075, 2015, doi: 10.1109/TCST.2015.2396473.
[25] B. Brogliato and A. Polyakov, "Digital implementation of sliding-mode control via the implicit method: A tutorial," *Int. J. Robust Nonlinear Control*, vol. 31, no. 9, pp. 3528–3586, Jun. 2021, doi: 10.1002/rnc.5121.
[26] O. Huber, V. Acary, and B. Brogliato, "Lyapunov stability and performance analysis of the implicit discrete sliding mode control," *IEEE Trans. Autom. Control*, vol. 61, no. 10, pp. 3016–3030, Oct. 2016, doi: 10.1109/TAC.2015.2506991.
[27] V. Acary, B. Brogliato, and Y. V. Orlov, "Chattering-free digital sliding-mode control with state observer and disturbance rejection," *IEEE Trans. Autom. Control*, vol. 57, no. 5, pp. 1087–1101, May 2012, doi: 10.1109/TAC.2011.2174676.
[28] F. A. Miranda-Villatoro, F. Castaños, and B. Brogliato, "Continuous and discrete-time stability of a robust set-valued nested controller," *Automatica*, vol. 107, pp. 406–417, Sep. 2019, doi: 10.1016/j.automatica.2019.06.003.
[29] R. Kikuuwe, T. Okada, H. Yoshihara, T. Doi, T. Nanjo, and K. Yamashita, "Nonsmooth quasistatic modeling of hydraulic actuators," 2021, *arXiv:2102.11381*.
[30] K. Murata, R. Kikuuwe, T. Okada, H. Yoshihara, T. Doi, T. Nanjo, and K. Yamashita, "Realtime simulation techniques for hydraulic excavators," in *Proc. 20th SICE Syst. Integr. Division Annu. Conf.*, 2019, pp. 2526–2531.
[31] R. Kikuuwe, N. Takesue, A. Sano, H. Mochiyama, and H. Fujimoto, "Admittance and impedance representations of friction based on implicit Euler integration," *IEEE Trans. Robot.*, vol. 22, no. 6, pp. 1176–1188, Dec. 2006, doi: 10.1109/TRO.2006.886262.
[32] R. Kikuuwe, T. Yamamoto, and H. Fujimoto, "Velocity-bounding stiff position controller," in *Proc. IEEE/RSJ Int. Conf. Intell. Robots Syst.*, Oct. 2006, pp. 3050–3055, doi: 10.1109/IROS.2006.282243.
[33] S. Jin, R. Kikuuwe, and M. Yamamoto, "Real-time quadratic sliding mode filter for removing noise," *Adv. Robot.*, vol. 26, nos. 8–9, pp. 877–896, 2012, doi: 10.1163/156855312X633011.

YUKI YAMAMOTO received the B.E. degree in mechanical engineering from Hiroshima University, Hiroshima, Japan, in 2020, where he is currently pursuing the master's degree with the Graduate School of Advanced Science and Engineering (Mechanical Engineering Program). His research interests include control engineering, dynamics identification, mechatronics, and force estimation of hydraulic actuators.

JINJUN QIU received the M.E. and Ph.D. degrees from Kyushu University, Fukuoka, Japan, in 2009 and 2012, respectively.

In 2018, he joined Kobelco Construction Machinery Company Ltd., Hiroshima, Japan. He is currently a member of the Automated System Engineering Group, the Advanced Technology Engineering Department, Kobelco Construction Machinery Company Ltd.

YOSHIKI MUNEMASA received the M.E. degree in mechanical engineering from the Tokyo University of Agriculture and Technology, Tokyo, Japan, in 2019.

He is currently a member of the Automated System Engineering Group, Advanced Technology Engineering Department, Kobelco Construction Machinery Company Ltd., Hiroshima, Japan.

TAKAYUKI DOI joined Kobelco Construction Machinery Company Ltd., Hiroshima, Japan, in 2006. He is currently the Group Leader of the Automated System Engineering Group, the Advanced Technology Engineering Department, Kobelco Construction Machinery Company Ltd. He is engaged in the development of hydraulic excavators electricity/control systems.

TAKAO NANJO received the M.E. degree in mechanical engineering from Kyushu University, Fukuoka, Japan, in 1992.

From 1992 to 2017, he was with Kobe Steel Ltd. In 2017, he joined Kobelco Construction Machinery Company Ltd., Hiroshima, Japan. He is currently the Senior Manager of the Data Driven System Engineering Group, Advanced Technology Engineering Department, Kobelco Construction Machinery Company Ltd.

Mr. Nanjo is a member of the Japan Society of Mechanical Engineers.

KOJI YAMASHITA received the M.Eng. degree in mechanical engineering from the Toyohashi University of Technology, Japan, in 1994.

From 1994 to 1999, he was with Kobe Steel Ltd. In 1999, he joined Kobelco Construction Machinery Company Ltd., Hiroshima, Japan. Since 2020, he has been a Visiting Professor with Hiroshima University, Japan. He is currently the General Manager of the Department of System and Component, Kobelco Construction Machinery Company Ltd.

RYO KIKUUWE (Member, IEEE) received the B.S., M.S., and Ph.D.(Eng.) degrees in mechanical engineering from Kyoto University, Kyoto, Japan, in 1998, 2000, and 2003, respectively.

From 2003 to 2007, he was an Endowed-Chair Research Associate with the Nagoya Institute of Technology, Nagoya, Japan. From 2007 to 2017, he was an Associate Professor with the Department of Mechanical Engineering, Kyushu University, Fukuoka, Japan. From 2014 to 2015, he was a Visiting Researcher with the Institut National de Recherche en Informatique et en Automatique (INRIA) Grenoble Rhône-Alpes, Saint Ismier, France. He is currently a Full Professor with the Graduate School of Advanced Science and Engineering, Hiroshima University, Hiroshima, Japan. His research interests include force control of robot manipulators, real-time simulation for physics-based animation, and engineering applications of differential inclusions.

Prof. Kikuuwe is a member of the Robotics Society of Japan, the Japan Society of Mechanical Engineers, the Society of Instrument and Control Engineers (Japan), and the Virtual Reality Society of Japan. He was a recipient of the Best Paper Award of Advanced Robotics, in 2013, and the Young Investigator Excellence Award from the Robotics Society of Japan, in 2005.